Chemosphere 378 (2025) 144388

Contents lists available at ScienceDirect

Chemosphere

journal homepage: www.elsevier.com/locate/chemosphere

Novel hemin-derived Fe/N–C magnetic catalyst for enhanced peroxymonosulfate activation and diclofenac degradation

Aaron Albert Aryee [a,b], Alam Venugopal Narendra Kumar [b], Won Sik Shin [b,*]

[a] Department of Chemistry, College of Basic and Applied Sciences, University of Ghana, Legon, Ghana
[b] School of Architecture, Civil, Environmental and Energy Engineering, Kyungpook National University, Daegu 41566, Republic of Korea

HIGHLIGHTS

- A new PA@Hem$_{700}$ catalyst was synthesized by a one-pot pyrolysis of polyacrylate and hemin.
- PA@Hem$_{700}$ exhibited high DCF degradation efficiency in both acidic and neutral pH.
- Interference of common anions are minimum in PA@Hem$_{700}$/PMS system.
- DCF degradation is mainly triggered by $^1O_2$ in the PA@Hem$_{700}$/PMS system.
- A correlation between PA@Hem$_{700}$/PMS degradation performance and pollutants log K_{ow} was observed.

GRAPHICAL ABSTRACT

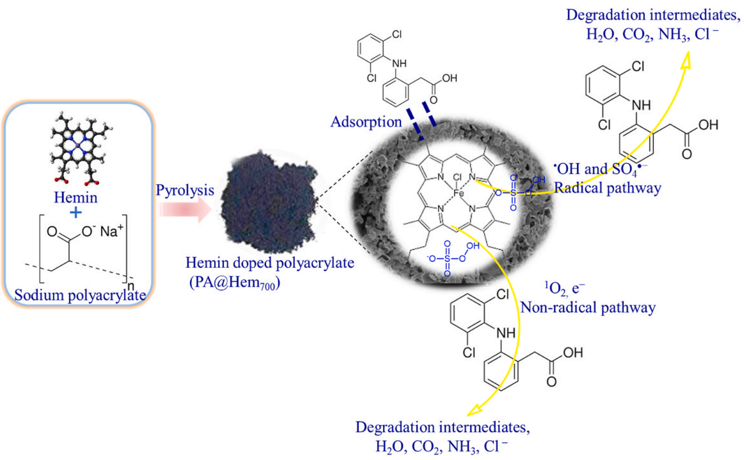

ARTICLE INFO

Handling editor: Jun Huang

Keywords:
Diclofenac
Fe/N–C catalyst
Peroxymonosulfate
Hemin
Polymer

ABSTRACT

In this study, Fe involved N-doped carbon catalysts labelled as PA@Hem$_x$ (x = pyrolysis temperature) was synthesized through a one-step pyrolysis of hemin (Hem) and polyacrylate (PA). The reported method enables high dispersion and exposure of both Fe and N active sites on PA derived carbon. The PA@Hem$_x$ samples were then used for peroxymonosulfate (PMS) activated diclofenac (DCF) degradation. Results from the characterization studies verified the successful incorporation of hemin in the composite. Approximately 99.2 % DCF degradation at pH = 6.01 was achieved in 60 min using 0.1 g L^{-1} PA@Hem$_{700}$ and 1.0 mM PMS. The pseudo-second-order kinetic model and Langmuir model were used to described the uptake and equilibrium process in DCF/PA@Hem$_{700}$ system. Scavenging and electron-spin-resonance studies showed a non-radical singlet oxygen species ($^1O_2$) dominates over $^{\bullet}OH$ and $SO_4^{\bullet-}$ radicals in the system. The role of electron transfer was also verified via chronoamperometry and electrochemical-impedance spectroscopy techniques. Furthermore, the PA@Hem$_{700}$/PMS remained highly active towards DCF degradation even in the presence of common anions, humic acid, and various water matrices. The developed catalyst exhibited a TOC removal of 65.8 %. The study also established the potential of PA@Hem$_{700}$/PMS to degrade other organic pollutants (e.g., tetracycline (TC),

---

* Corresponding author.
E-mail address: wshin@knu.ac.kr (W.S. Shin).

https://doi.org/10.1016/j.chemosphere.2025.144388
Received 23 December 2024; Received in revised form 26 February 2025; Accepted 3 April 2025
Available online 10 April 2025

simazine (SIM), and sulfamethoxazole (SMX)). The results from this study are expected to advance research on synthesizing other novel polymer-based Fe/N–C catalysts for degrading organic pollutants.

1. Introduction

Water treatment continues to garner increasing attention owing to the significant role of clean water in the functioning of the environment. This increased attention could be attributed to the continuous detection of persistent organic pollutants in water resources (Aryee et al., 2022; Li et al., 2024). Recently, the demand for pharmaceutical has upsurged due to an increase in diseases and other adverse factors against human health (Cangola et al., 2024). For example, diclofenac (DCF) has been widely administered to humans, domestic animals, and livestock to treat non-rheumatoid diseases and inflammation. Its demand is expected to rise, as can deduced from DCF sales, which have been set to reach $6.1 billion by 2027 with a compound annual growth rate of 3.9 %. However, an average of 65 % of administered DCF (oral dosage) is excreted through urine and end up at wastewater treatment plants (WWTPs) with concentrations ranging from ng L^{-1} – μg L^{-1} (Alessandretti et al., 2021; Sathishkumar et al., 2020). The inability of these WWTPs to completely discard DCF from the systems, coupled with their discriminate disposal as solid wastes, could account for their presence in surface water. For instance, the concentration of DCF in surface water, groundwater, tap water and wastewater were found to be 1.2×10^{-3}, 0.38×10^{-3}, 0.01×10^{-3} and 4.7×10^{-3} mg L^{-1}, respectively (Aguinaco et al., 2012; Lu et al., 2017). In addition, DCF has been associated with adverse health effects such as gastrointestinal bleeding, cardiovascular disease, and kidney ailments in humans; hence, their elimination from the aquatic system is crucial (Sathishkumar et al., 2020).

Consequently, several remediation techniques have been developed and applied to address DCF contamination (Alessandretti et al., 2021; Dai et al., 2024; Su et al., 2018). Among these techniques, several reports have established the prospects of advanced oxidation process (AOP) for mitigating organic pollutants (Giannakis et al., 2021; Hassani et al., 2023; Mustafa and Hama Aziz, 2023). This could be attributed to the ease associated with the application of AOP and the remarkable stability and convenient transportation of oxidants (either peroxodisulfate (PDS) or peroxymonosulfate (PMS)). However, PMS's remarkable benefits, including its high reactivity and lower cost, may account for its extensive application in AOP. Several reports have documented various strategies for PMS activation. Amongst these, carbonaceous materials have been widely explored to determine an alternative use for this large bioresource typically considered waste materials (Hao et al., 2023). A thorough literature review verifies the potential of landfill waste as precursors for synthesizing catalysts capable of degrading organic pollutants through PMS activation. For instance, Annamalai and Shin (2023) reported the degradation of DCF using a catalyst based on boron-doped biochar derived from *Undaria pinnatifida* (algae biomass). This catalyst could achieve 100 % degradation of DCF within 30 min, which was attributed to both radical and non-radical mechanisms.

The increasing detection of microplastics in the environment is attributable to their widespread use and advancements in analytical techniques enabling trace-level detection (Alimi et al., 2021; Shukla et al., 2022). Sodium polyacrylate (PA), a polymer that is synthesized from acrylate monomers, has been widely applied in consumer products such as napkins, diapers, and face masks. This could be attributed to its unique properties, such as optimal mechanical stability and high heat resistance (Masud and Shin, 2024). In addition, carboxylic functional groups and sodium atoms facilitate its ability to function as a super-absorbent and absorb 100–1000 times its mass in water. However, PA, classified as a synthetic plastic, persists in the environment due to its non-biodegradability, thereby fostering environmental pollution. Studies on determining alternative uses for spent materials containing polyacrylate have been reported to address this concern. For instance, Lee et al. (2023) developed a carbonate-enriched carbon catalyst based on diapers for activating PMS in trimethoprim (TMP) degradation. This novel catalyst can achieve 95 % TMP removal efficiency within 180 min due to the ability of its carbonate ions (CO_3^{2-}) to trigger the generation of singlet oxygen species ($^1O_2$) from PMS. Masud and Shin (2024) explored the oxidative removal of TMP using an N-doped catalyst (N–$SAPC_{800}$) based on the pyrolysis of urea-modified PA. Analysis of the underlying mechanism for the N–$SAPC_{800}$/PMS system suggested the degradation of TMP occurs via a non-radical pathway. These reports indicate the feasibility of utilizing polyacrylate in developing efficient materials with broad prospects in wastewater treatment.

In this study, we propose a promising approach for fabricating an Fe/N–C-type composite catalyst for PMS activation by one-step pyrolysis of hemin (as N and Fe source) and PA, highlighting its potential for future PA waste repurposing. The Fe and N–C sites were formed by combining hemin and PA at high weight ratio (1:20). As a result, we achieved a uniform distribution of Fe and N sites on the PA-derived carbon support. The adopted strategy enables high active site exposure to boost the catalytic activity. Also, the surface analysis results showed a huge variation in morphology of simple PA-derived carbon and the typical composite catalyst (PA@Hem_{700}). Its catalytic activity was assessed through DCF degradation under different operating conditions. Furthermore, the feasibility of the catalyst for practical applications was explored by investigating the influence of co-existing anions, humic acid (HA), and various water matrices on the degradation system. A plausible degradation mechanism was proposed based on quenching experiments, electron spin resonance (ESR) analysis, and electrochemical studies. The DCF degradation pathway was determined via the ultra-high-performance liquid chromatography-mass spectrometer. To the best of our knowledge, this is the first report on the synthesis of an Fe/N–C catalyst based on polyacrylate and hemin for PMS activated DCF degradation. The results obtained from this study may lead to the development of efficient materials derived from low-biodegradable plastics for organic pollutant remediation.

2. Methodology

2.1. Chemicals

The chemicals utilized in this study were of analytical grade. Details of these chemicals are provided in **Text S1** of the supplementary section.

2.2. Preparation and characterisation of catalysts

The PA@Hem_x catalysts were prepared based on our previous reports (Aryee et al., 2024; Masud and Shin, 2024). Sodium polyacrylate (5 g) and hemin (0.25 g) were thoroughly mixed and ground in a mortar. The obtained mixture was transferred into a quartz boat and pyrolyzed in a tubular furnace at various temperatures (i.e., 700, 800, and 900 °C) for 2 h under N_2 gas at a heating rate of 5 °C min^{-1}. The obtained material was washed with ethanol and deionized water until the pH of the filtrate was near neutral and then dried in an oven overnight at 60 °C. The dried catalyst was then ground and sieved through a 75 μm mesh, transferred into air-tight containers, and labelled PA@Hem_{700}, PA@Hem_{800}, and PA@Hem_{900}. For comparison, PA_{700} was synthesized by a similar method at a pyrolysis temperature of 700 °C using only PA as the precursor. Fig. 1 is a schematic illustrating the synthesis of PA@Hem_x.

The physicochemical characteristics of the synthesized materials was assessed using X-ray photoelectron spectroscopy (XPS), Fourier transform infrared (FTIR) spectroscopy, X-ray diffractometry (XRD), Raman spectroscopy, vibrating sample magnetometer (VSM), scanning electron microscopy (SEM), and energy dispersive X-ray spectroscopy (EDS). Details of these studies are presented in the supplementary section (**Text S2**).

2.3. Adsorption and catalytic degradation experiment

The batch method was employed for adsorption and degradation experiments. In the adsorption studies, 0.1 g L^{-1} of PA@Hem$_x$ was added to 125 mL Erlenmeyer flasks containing 50 mL DCF at various concentrations (i.e., 5, 10, 15, 20. and 30 mg L^{-1}) with an unadjusted pH (i.e., 6.01) and allowed to react for 60 min at 200 rpm. After this period, the PA@Hem$_x$ material was separated using a magnet, and the solution was filtered through a 0.22 μm polytetrafluoroethylene (PTFE) filter. The residual concentration of DCF in these solutions was then measured using high-performance liquid chromatography (HPLC), with the conditions detailed in **Text S3**. The adsorption capacity (q, mg g^{-1}) and removal percentage (η, %) were assessed, as explained in **Text S4**.

In the catalytic degradation experiment, 0.1 g L^{-1} PA@Hem$_x$ was added to 50 mL of 10 mg L^{-1} DCF solution, after which 0.5 mL of PMS (100 mM) was added to initiate the degradation process. At given time intervals, 1 mL of the sample was extracted and added to 1 mL of 20 mM thiosulfate solution to terminate the reaction. After filtering through the PTFE filter, the remaining DCF in this solution was measured as described above. The pseudo-first-order kinetic model (PFKOM), as shown in Eq. (1), was employed to describe the catalytic degradation of DCF.

$$\ln\left(\frac{C_t}{C_0}\right) = -kt \tag{1}$$

where C_0 and C_t correspond to the initial and final concentrations of DCF, respectively, while k represents the reaction rate constant of PFKOM ($\min^{-1}$).

All experiments were performed in triplicates to ensure the reproducibility of this study's results.

3. Results and discussions

3.1. Physicochemical properties of PA@Hem$_x$ catalyst

The crystallinity of the synthesized samples was evaluated using X-ray diffraction. The diffraction patterns of PA@Hem$_x$ in Fig. 2a show peaks at 2θ = 26.2 and 45.0° that corresponds to (0 0 2) and (1 1 1) crystalline planes of carbon (Masud and Shin, 2024; Pereira et al., 2021). Compared to PA$_{700}$, the number of diffraction peaks notably reduced, suggesting that adding hemin significantly improved the crystallinity of the synthesized catalysts. In addition to that, some peaks corresponding to the spinel structure of Fe_3O_4 and Fe_2O_3 were observed in PA@Hem$_x$, suggesting the formation of a magnetic composite (Aryee et al., 2021). The degree of graphitization and the presence of surface defects were further analysed using Raman spectroscopy. The Raman spectra for PA$_{700}$ and PA@Hem$_x$ samples (i.e., PA@Hem$_{700}$, PA@Hem$_{800}$, and PA@Hem$_{900}$) were analysed and showed in Fig. S1, while the associated parameters are presented in Table S1. From the spectral analysis , the primary peaks found at 1357.0–1373.4 cm^{-1} and 1585.7–1596.6 cm^{-1} are mainly assigned to D (D1) and G bands, that corresponds to the vibrations of disordered graphitic structures and graphitic lattices, respectively (Masud and Shin, 2024; Pereira et al., 2021). Furthermore, the calculated I_D/I_G ratio for these samples demonstrated that PA@Hem$_{700}$ exhibited the highest value (i.e., 1.07), suggesting it has higher surface defects (Bae et al., 2024). The SEM images of PA$_{700}$ and PA@Hem$_{700}$ are presented in Fig. 2b and c. The morphology of PA$_{700}$ was observed to be relatively smooth, with some pores. Upon hemin addition, the amount of surface pores was enhanced, and the surface of the resultant material was rougher. The elemental mapping images obtained from the EDS are presented in Fig. S2. The PA$_{700}$ contained C, N, and O, evenly distributed on its surface. However, an additional element, Fe, was found in PA@Hem$_{700}$ indicating the successful loading of hemin on the catalyst.

The elemental composition and oxidation state on PA$_{700}$ and PA@Hem$_{700}$ were further investigated via XPS analysis. The percentages of the primary elemental composition are presented in Table S2. The survey spectra of PA$_{700}$ exhibited peaks at 283.73 and 531.17 eV, representing C 1s and O 1s, respectively (Fig. 2d). Upon modification with hemin, new peaks at 398.72 and 710.35 eV were emerged, which can be assigned to N and Fe atoms (Aryee et al., 2024). A detailed analysis of these peaks was carried out using the XPS Peak 41 software and the results shown in Fig. S3. The analysis of the C 1s peak on PA$_{700}$ revealed three peaks at 283.50 (C–C), 284.25 (C=C) and 289.18 eV (C=O) (data not shown). Peaks at similar binding energy were also observed in PA@Hem$_{700}$ along with C–N peak which appeared at 287.79 eV (Ayiania et al., 2020). In the deconvoluted O 1s spectra, an additional peak at 529.95 eV was observed which can be assigned to Fe–O in PA@Hem$_{700}$ further corroborating the successful incorporation of Fe in PA. Furthermore, the deconvoluted N 1s peak on PA@Hem$_{700}$ exhibited two peaks at 397.04 and 398.86 eV which could be ascribed to pyrrolic–N and pyridinic–N respectively. Characteristic peaks of Fe 2p were observed at 710, 712.38 and 725.05 eV corresponding to Fe^{2+} $2p_{3/2}$, Fe^{3+} $2p_{3/2}$, and Fe^{3+} $2p_{1/2}$, respectively (Aryee et al., 2024).

The magnetic properties of PA$_{700}$ and PA@Hem$_{700}$ samples were studied using the VSM technique. The results show that PA$_{700}$ itself has no magnetic property, whereas, the PA@Hem$_{700}$ exhibited a magnetization value of 3.97 emu g^{-1} (Fig. 2e). This clearly indicates the

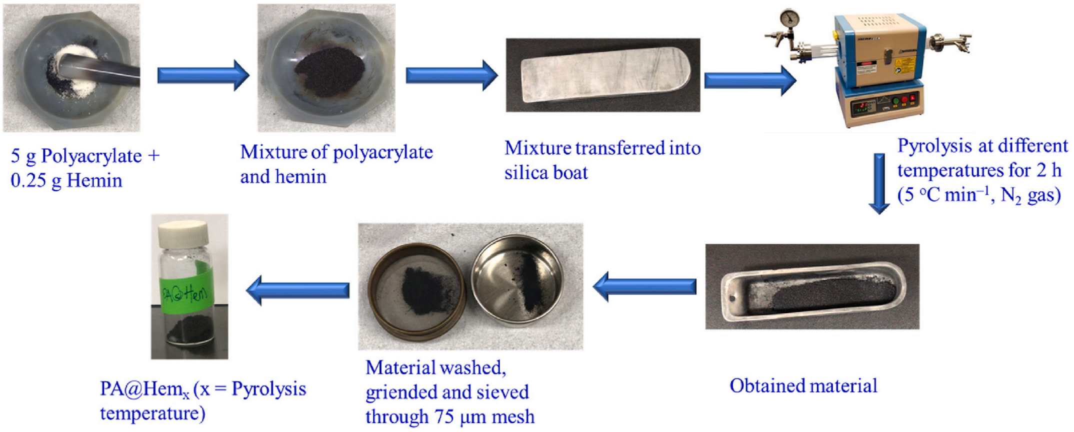

Fig. 1. Schematic diagram illustrating the synthesis of PA@Hem$_x$.

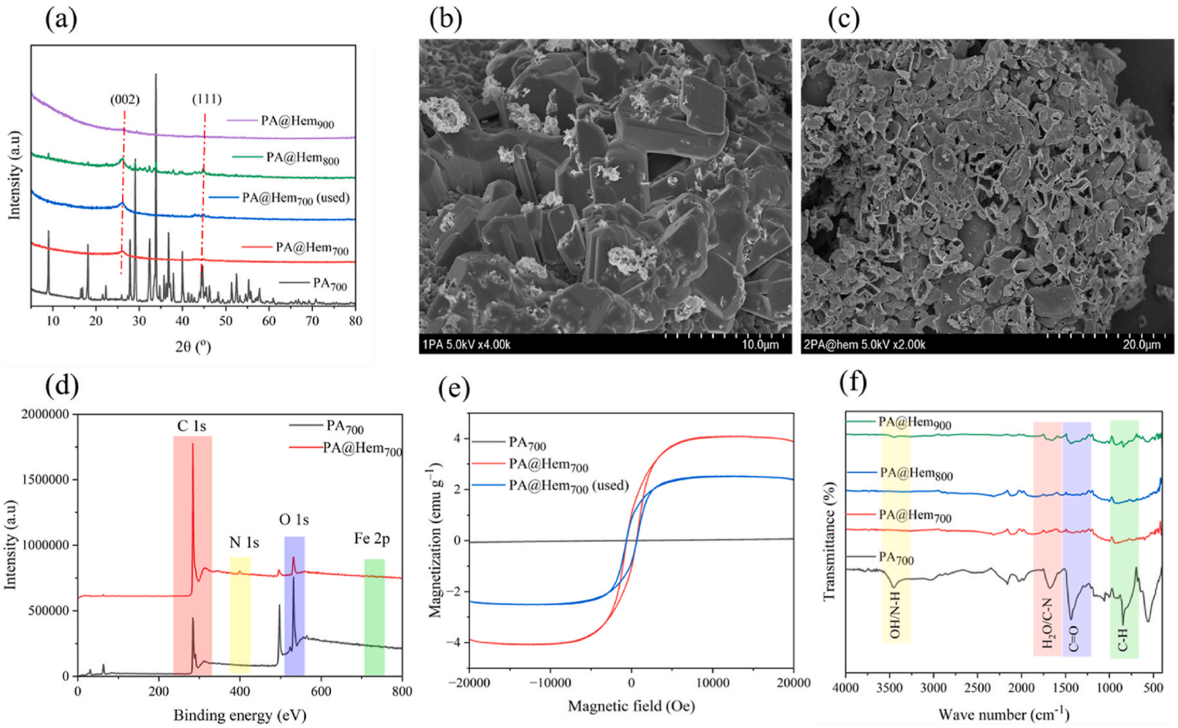

Fig. 2. Results of characterization studies: (a) XRD pattern of synthesized materials; SEM image of (b) PA_{700} (c) $PA@Hem_{700}$; (d) XPS wide scan for PA_{700} and $PA@Hem_{700}$; (e) Magnetic hysteresis curves of PA_{700} and $PA@Hem_{700}$ (before and after oxidation study); (f) FTIR spectrum for PA_{700} and $PA@Hem_x$ samples.

formation of carbon magnetic composite catalyst upon hemin addition. Notably, the $PA@Hem_{700}$ sample after DCF degradation still exhibits a magnetic property as seen from its magnetization value of 2.43 emu g^{-1}. Later observation reveals the feasibility of $PA@Hem_{700}$ retrieval from a solution using a magnet, which is relatively easier and less expensive than the filtration technique. Identification of chemical functionals that present in these samples are important to relate their catalytic properties. Therefore, FTIR spectroscopy was adopted to analyse these functional groups (see Fig. 2f). The FTIR spectrum of PA_{700}, displayed two intense bands at 3454.7 and 1677.8 cm^{-1}, which represent –OH stretching and H_2O scissoring vibrations, respectively. In addition, the peak at 1436.4 cm^{-1} can be attributed to the symmetrical stretching vibrations of the carboxylate anion (Di Maggio et al., 2019). With the introduction of hemin, the C=O peaks were supressed significantly in the $PA@Hem_x$ samples suggesting the ability of hemin to alter the surface properties of PA_{700}. This is attributed to Fe that present in hemin which forms stable complexes with carbonyl groups during pyrolysis and facilitate carbon dioxide release (Boitrel et al., 2017). Consequently, the carbon framework in $PA@Hem_x$ undergoes significant carbon restructuring, resulting in a minimal presence of surface functional groups. Furthermore, introducing N atoms from hemin could infer the presence of N–H and C–N stretching vibrations at approximately 3448.4 and 1668.2 cm^{-1}, respectively (Han et al., 2018). A similar observation was made by Masud and Shin (2024) in their study on the synthesis of PA-based carbon catalyst in the present of urea.

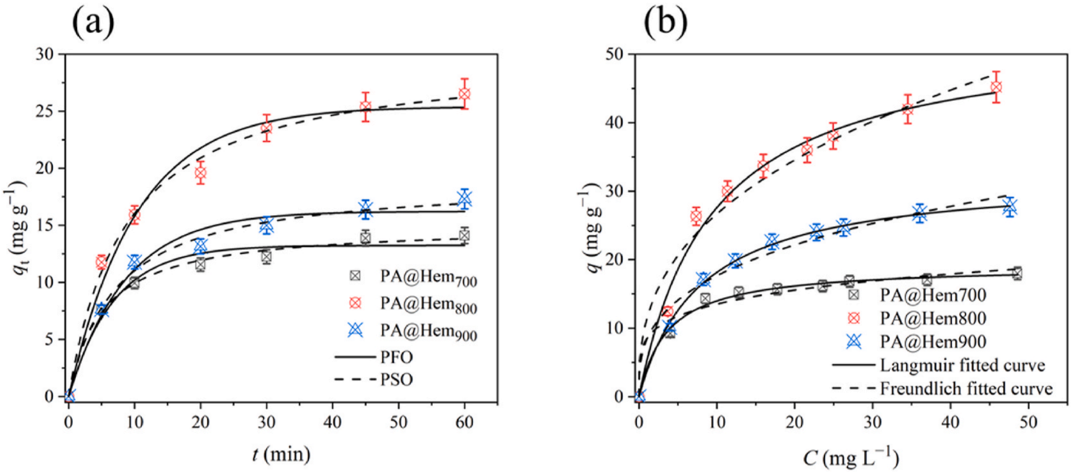

Fig. 3. (a) Adsorption kinetics of DCF on $PA@Hem_x$ samples; solid and dashed lines represent PFO and PSO kinetic models, respectively. (b) Adsorption isotherm of DCF onto $PA@Hem_x$; solid and dashed lines represent the Langmuir and Freundlich isotherm models, respectively. (Experimental conditions: $[Catalyst]_0 = 0.1$ g L^{-1}, $[DCF]_0 = 10$ mg L^{-1}, pH = 6.01 (unadjusted)).

3.2. Adsorption kinetics

The uptake of DCF onto PA@Hem$_x$ samples was studied, and the results are presented in Fig. 3a. The adsorption capacities of PA@Hem$_{700}$, PA@Hem$_{800}$, and PA@Hem$_{900}$ towards DCF after 60 min were 14.1, 26.5, and 17.3 mg g^{-1}, respectively. To further understand the probable mechanisms underlying the adsorption process, the non-linear forms of the pseudo-first-order (PFO) and pseudo-second-order (PSO) kinetic models, as expressed in Eqs. S3 and S4, respectively, were fitted to the experimental data. As illustrated in Fig. 3a, the fitted curves by both models were close to the experimental data, suggesting their ability to describe the adsorption process relatively. The regression coefficient (R^2) value and sum squared of error (*SSE*) values were then employed to determine the best fitting model. As presented in Table S3, the PSO model exhibits higher R^2 values (i.e., $R^2 \geq 0.994$) and smaller *SSE* values (i.e., $SSE \leq 2.60$), indicating its remarkable suitability to describe the adsorption process. This observation indicates that the adsorption process is primarily dependent on the interaction between the available adsorption sites and DCF molecules, which are controlled by chemisorption forces (Aryee et al., 2021; Wang and Guo, 2020a).

3.3. Adsorption isotherm

Isotherm experiments were performed to investigate the interaction between the DCF and the catalytic surface. From Fig. 3b, it is clear that the adsorption capacity of PA@Hem$_x$ samples increased with an increase in initial DCF concentration. This could be attributed to the ability of DCF molecules and the available active sites to form a concentration gradient that can address resistance to the adsorption process (Hu and Han, 2019; Liu et al., 2020). As described in **Text S4**, the Langmuir and Freundlich models were fitted to the equilibrium data to understand the adsorption process and the values of the associated parameters are presented in Table S3. The maximum monolayer adsorption capacity ($q_{\max}$) according to the Langmuir model was determined to be 19.1, 53.5, and 32.4 mg g^{-1} for PA@Hem$_{700}$, PA@Hem$_{800}$, and PA@Hem$_{900}$, respectively. The obtained *N* values from the Freundlich model were between 0 and 1, confirming the feasibility and efficiency of the adsorption process (Gu et al., 2019; Wang and Guo, 2020b). In addition, the K_F values from the Freundlich model, which indicate the affinity of the adsorbent for the adsorbate, were recorded to be 8.46, 11.3, and 8.32 ([mg g^{-1}] [mg L^{-1}]$^{-N}$) for PA@Hem$_{700}$, PA@Hem$_{800}$, and PA@Hem$_{900}$, respectively (Amrutha et al., 2023; Wang and Guo, 2020b). Furthermore, the R^2 values associated with the Langmuir model ($0.989 \leq R^2 \leq 0.999$), as presented in Table S3, were determined to be higher than those recorded for the Freundlich model ($0.968 \leq R^2 \leq 0.976$), suggesting its remarkable suitability in describing the adsorption process. The suitability of this model suggests the formation of monolayer on the surface of the adsorbent and that the process is mainly controlled by chemisorption forces (Aziz et al., 2024). This corroborates the results from the kinetic study.

3.4. Catalyst selection

The influence of temperature on PA@Hem$_x$ catalytic efficiency was assessed to select the optimum pyrolysis temperature for catalyst preparation. Upon screening, we found the DCF removal efficiencies of PA@Hem$_{700}$, PA@Hem$_{800}$, and PA@Hem$_{900}$ via adsorption were 14.1 %, 26.5 %, and 17.3 %, respectively (Fig. 4a). With the introduction of 1.0 mM PMS into the system, the removal efficiency of PA@Hem$_{700}$, PA@Hem$_{800}$, and PA@Hem$_{900}$ increased dramatically to 99.2, 99.9, and 70.3 %, respectively. In addition, the associated degradation rate constant (k) obtained from fitting the PFOKM was determined to be 7.36×10^{-2}, 8.96×10^{-2} and 2.43×10^{-2} min^{-1} for PA@Hem$_{700}$, PA@Hem$_{800}$ and PA@Hem$_{900}$, respectively (Fig. S4). Although PA@Hem$_{800}$ exhibited a slightly higher degradation rate, PA@Hem$_{700}$ was selected as the catalyst for subsequent studies. It is based on the marginal difference in degradation efficiency compared with PA@Hem$_{800}$ and its lower pyrolysis temperature, which may have some environmental and economic benefits. To verify the role of Fe/N as contributed by the hemin, the removal efficiency of PA$_{700}$ (without hemin doping) was also

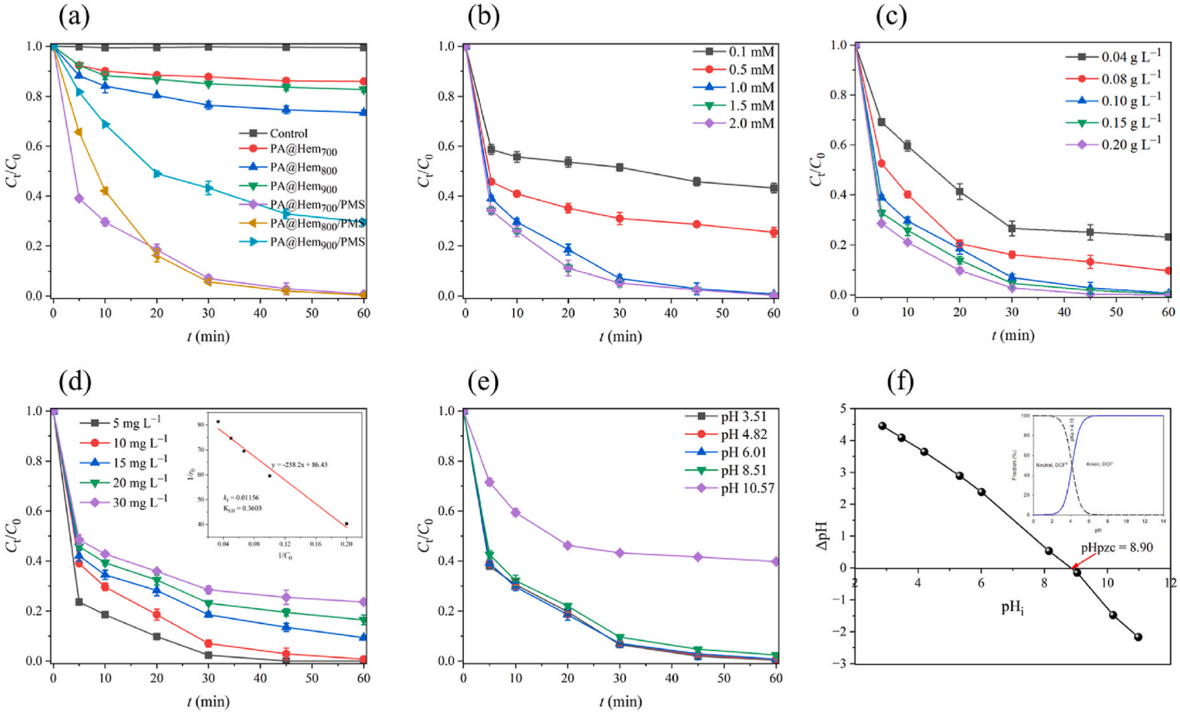

Fig. 4. (a) Comparison of different systems towards DCF removal; (b) Effect of PMS concentration; (c) Effect of catalyst dose; (d) Effect of initial DCF concentration (inset: L-H kinetic model); (e) Effect of initial DCF solution pH; (f) Analysis of pH$_{pzc}$ of PA@Hem$_{700}$ (inset: pK$_a$ value of DCF). (Experimental conditions: $[\text{Catalyst}]_0 = 0.1$ g L^{-1}, $[\text{DCF}]_0 = 10$ mg L^{-1}, $[\text{PMS}]_0 = 1.0$ mM, pH = 6.01 (unadjusted)).

investigated. Although the removal efficiency of PA_{700} (via adsorption) was 9.8 %, it increased to 32.8 % in the PA_{700}/PMS system. This was significantly lower than that recorded for the $PA@Hem_{700}$/PMS, thus verifying the major role of the Fe/N moiety in the degradation process.

3.5. DCF degradation in the $PA@Hemin_{700}$/PMS system

3.5.1. Effect of PMS concentration

The influence of PMS on the degradation process is provided in Fig. 4b. Here, at a fixed catalyst dose of 0.1 g L^{-1}, the DCF degradation values were 56.7 %, 74.5 %, 99.2 %, 99.7 %, and 100 % at PMS dosages of 0.1, 0.5, 1.0, 1.5, and 2.0 mM, respectively. A noticeable improvement in DCF removal was witnessed when the PMS dosage increased from 0.1 to 1.0 mM; however, a marginal change was observed beyond this point. This could be attributed to the higher amount of ROS generated at higher PMS doses (Aryee et al., 2024). As described in **Text S5**, the amount of ROS generated under these conditions were 6.15×10^{-3}, 1.08×10^{-2}, 3.68×10^{-2}, 3.90×10^{-2}, and 3.90×10^{-2} mg min^{-1}, respectively. However, beyond 1.0 mM of PMS, negligible change was detected in the rate of ROS generation. This could be attributed to the ability of excessive PMS to scavenge $^{\bullet}OH$ and $SO_4^{\bullet-}$, and generate less reactive species, as expressed in Eqs. 2 and 3 (Wu et al., 2023). Furthermore, only 8.1 % of DCF was discarded when the degradation was carried out with only PMS (1.0 mM). It reveals the limited ability of PMS to generate radicals without a catalyst. Consequently, 1.0 mM of PMS was selected as the optimum dosage for subsequent studies.

$$HSO_5^{\cdot-} + SO_4^{\cdot-} \rightarrow SO_5^{\cdot-} + SO_4^{2-} + H^+ \tag{2}$$

$$HSO_5^{\cdot-} + {}^{\cdot}O\,H \rightarrow SO_5^{\cdot-} + H_2O \tag{3}$$

3.5.2. Effect of $PA@Hemin_{700}$ concentration

The impact of the catalyst dose on DCF degradation is shown in Fig. 4c. The DCF removal efficiency was approximately 76.8, 90.2, 99.2, 99.8, and 100 % for 0.04, 0.08, 0.1, 0.15, and 0.2 g L^{-1} $PA@Hem_{700}$, respectively. The associated degradation rate constant obtained from fitting the PFKOM to the data increased from 3.11×10^{-2} to 1.13×10^{-1} min^{-1} as the $PA@Hem_{700}$ concentration increased from 0.04 to 2.0 g L^{-1} (Table S4). This improvement in removal efficiency with an increase in catalyst dose could be due to the increase in the Fe/N–C active sites, which facilitates PMS activation to generate ROS, as presented in (Eqs. 4 and 5) (Song et al., 2023). To verify this assertion, the generation rate of ROS relative to the catalyst concentration was investigated. The ROS generation rates at $PA@Hem_{700}$ concentrations of 0.04, 0.08, 0.1, 0.15, and 0.2 g L^{-1} was 1.56×10^{-2}, 2.15×10^{-2}, 3.68×10^{-2}, 4.10×10^{-2}, and 5.68×10^{-2} mg min^{-1}, respectively. It is further evident that an increased catalyst dose resulted in higher number of ROS generation due to the greater availability of Fe/N–C sites. Based on these results, 0.1 g L^{-1} was selected as an optimum catalyst dose owing to the marginal difference in removal efficiency beyond this point.

$$Fe / N - C + HSO_5{}^{-} \rightarrow 2SO_4^{\cdot-} + OH^- \tag{4}$$

$$2HSO_5{}^{-} + Fe / N - C \rightarrow SO_4^{2-} + SO_4^{\cdot-} + {}^{\cdot}O\,H \tag{5}$$

3.5.3. Effect of DCF concentration

Fig. 4d illustrates the effect of initial DCF concentration on the degradation process. With an increase in DCF concentration from 5 to 30 mg L^{-1}, the removal percentage of DCF decreased from 100 to 76.3 % within 60 min. The initial degradation rate (r_0) at the studied concentrations was then analysed to fit the Langmuir-Hinshelwood (L–H) kinetic model (**Text S6**). The L–H kinetic model can be utilised to evaluate the heterogeneous catalysis involved in DCF adsorption and degradation. From this analysis, a linear correlation ($R^2 = 0.979$) was observed by plotting $1/r_0$ vs $1/C_0$ (Fig. 4d (inset)). In addition, the calculated apparent rate constant (k_r) and adsorption equilibrium constant (K_{LH}) were 0.012 mg L^{-1} min^{-1} and 0.363 L mg^{-1}, respectively. The significantly higher K_{LH} value compared to the k_r, suggests that the DCF degradation was primarily on the surface of $PA@Hem_{700}$ (Annamalai and Shin, 2023; Bae et al., 2024; Masud and Shin, 2024).

3.5.4. Effect of DCF solution pH

The pH of a solution is a crucial parameter in advanced oxidation processes as it influences the catalytic performance and oxidation states of the catalyst (Peng et al., 2021). As illustrated in Fig. 4e, the catalyst exhibited an excellent DCF degradation efficiency within a broad pH range. Notably, under acidic (pH = 3.51), slightly acidic (pH = 4.82), and near neutral (pH = 6.01) conditions, the catalyst achieved over 99 % of DCF degradation. Under mild alkaline conditions (pH = 8.51), the degradation efficiency was slightly reduced to 97.6 %. However, the degradation efficiency of the system was significantly reduced to 60.2 % when the initial pH was increases to 10.57.

To understand this, the interaction between the $PA@Hem_{700}$ and the DCF was investigated by comparing the point of zero charge (pH_{pzc}) and speciation profiles of DCF. Based on our measurements that described in **Text S7**, the pH_{pzc} of $PA@Hem_{700}$ was determined to be 8.90 (Fig. 4f), suggesting the catalytic surface is positively and negatively charged below and above this point, respectively. However, majority of DCF exists in molecular state below the pK_a (=4.15) and the anionic form dominates above the pK_a (Fig. 4f (inset)). At acidic conditions (pH 3.51), $PA@Hem_{700}$ is positively charged, whereas DCF is neutral, suggesting that the adsorption process is primarily controlled by hydrophobic interactions and/or hydrogen bonding (Annamalai and Shin, 2023). Above pH 3.5 (i.e., $4.18 < pH < 10.57$), the electrostatic attraction may be the dominant mechanism owing to DCF's anionic nature and the positively charged $PA@Hem_{700}$ (Zhang et al., 2023). The major reduction in degradation efficiency recorded at pH 10.57 could be attributed to the enhanced electrostatic repulsion that exists between the negatively charged $PA@Hem_{700}$ surface and the anionic DCF molecule (Zhang et al., 2023). Under strong alkaline conditions, HSO_5^- mainly exists as SO_5^-, which possesses a lower oxidation potential (Masud et al., 2023). Furthermore, the tendency of Fe ions to be transformed into iron hydroxides and that of PMS to decompose into O_2 and SO_4^{2-} may all contribute to the lower degradation efficiency recorded under this condition (Aryee et al., 2024; Li et al., 2017).

3.6. Mechanisms underlying the catalytic degradation in $PA@Hemin_{700}$/PMS system

3.6.1. Determination of reactive oxygen species

Scavenging experiments and ESR analysis were performed to assess the types of ROS generated in the $PA@Hem_{700}$/PMS system. For this, scavenging agents such as *tert*-butyl alcohol (TBA), phenol (PhOH), and L-histidine (LHD) were utilised to detect the presence of $^{\bullet}OH$, $SO_4^{\bullet-}$, and $^1O_2$ species, respectively, (Annamalai and Shin, 2023; Masud and Shin, 2024). As illustrated in Fig. 5a, the introduction of TBA and PhOH reduced the degradation efficiency of the system to 97.6 and 89.5 %, respectively suggesting that although $^{\bullet}OH$ and $SO_4^{\bullet-}$ were generated in the system, their role in the degradation process was limited. The ESR technique was further applied to verify these results. As illustrated in Fig. 5b, a strong signal of 1:2:1:2:1:2:1 ratio was observed in the $PA@Hem_{700}$/PMS system when 5,5-dimethyl-1-pyrroline N-oxide (DMPO) was employed as a spin-trapping agent. This verifies the presence of $^{\bullet}OH$ and $SO_4^{\bullet-}$ in the system (Aryee et al., 2023). In addition, no peaks in PA_{700}/PMS suggest that the production of these radicals was primarily due to the hemin in the composite (Jiang et al., 2024).

The introduction of LHD resulted in a significant reduction in DCF degradation efficiency of the system (i.e., 58.6 %). These results indicate that the contribution of the $^1O_2$ supersedes that of the radical pathway in the $PA@Hem_{700}$/PMS system (Bae et al., 2024; Masud and Shin, 2024; Zhang et al., 2020). To assess the contribution of the superoxide radical

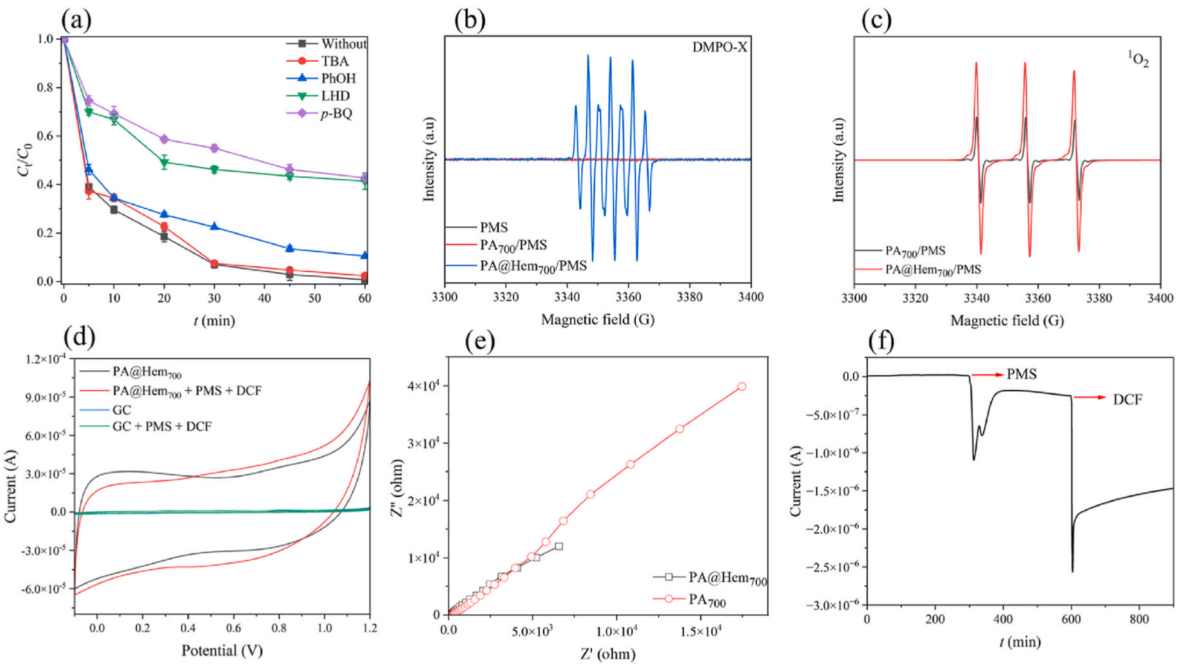

Fig. 5. (a) Effect of scavenging agents on the degradation of DCF in the $PA@Hem_{700}$/PMS system; ESR spectra in $PA@Hem_{700}$/PMS system with (b) DMPO and (c) TEMP; (d) CV response of bare GC electrode and $PA@Hem_{700}$ modified GC electrodes at different conditions; (e) EIS spectra of PA_{700} and $PA@Hem_{700}$; (f) the *i-t* curve of $PA@Hem_{700}$. (Experimental conditions: $[\text{Catalyst}]_0 = 0.1$ g L^{-1}, $[\text{DCF}]_0 = 10$ mg L^{-1}, $[\text{PMS}]_0 = 1.0$ mM, pH = 6.01; $[\text{TBA}]_0 = 250$ mM, $[\text{PhOH}]_0 = 0.5$ mM, $[\text{p-BQ}]_0 = [\text{LHD}]_0 = 5.0$ mM, $[\text{DMPO}] = [\text{TEMP}] = 100$ mM; $[Na_2SO_4]_0 = 100$ mM).

($O_2^{\bullet -}$) in the degradation process, para-benzoquinone (p-BQ) was employed as the scavenging agent. From the data, the impact of p-BQ was similar to that of LHD, suggesting it is the principal route for generating $^1O_2$ in the system, as illustrated in Eq. (6) (Aryee et al., 2023).

$$O_2^- + 2H_2O \rightarrow H_2O_2 + 2OH^- + {}^1O_2 \tag{6}$$

The ESR analysis in Fig. 5c, further confirmed the presence of $^1O_2$ in $PA@Hem_{700}$/PMS system. Evidently, the $^1O_2$ signal peaks generated in the $PA@Hem_{700}$/PMS system in the presence of 2,2,6,6-tetramethylpiperidine (TEMP) were higher than those of the PA_{700}/PMS system. This indicates that the presence of hemin in the composite and the increased surface defects may significantly contribute to generating $^1O_2$. Masud and Shin (2024) made similar observations in their study on the degradation of trimethoprim using an N-doped polymer based on urea and sodium acrylate as precursors. The report suggested that the generated $^1O_2$ species was due to the presence of N-doped graphitic carbon and surface defects in the catalyst.

3.6.2. Electrochemical studies

The role of electron transfer mechanisms in the degradation study was further assessed using electrochemical methods, as presented in **Text S3.** First, the cyclic voltametric response of $PA@Hem_{700}$ modified electrodes were compared with the unmodified GC electrodes in the presence of PMS and DCF (Fig. 5d). The curves of $PA@Hem_{700}$ electrode clearly displayed an increase in the oxidation current in the presence of oxidant and pollutant. The observed low current response is attributed to its high charging current contribution compared with GC electrode. The electrochemical impedance spectroscopy measurement of PA_{700} and $PA@Hem_{700}$ (Fig. 5e) revealed that the charge transfer resistance in $PA@Hem_{700}$ was lower than PA_{700} is due to the high graphitization (Annamalai and Shin, 2023) and the involvement of Fe_3O_4 in the carbon. In addition, results from the chronoamperometry (*i-t*) study, as illustrated in Fig. 5f, indicate that a smooth current was measured for the catalyst-coated electrode until 300 s when PMS was injected into the system. At this point, the current dropped and stabilized to 1.06 μA, forming a meta-stable complex between the $PA@Hem_{700}$ and PMS surfaces (Masud et al., 2023) With the further addition of DCF, the current was further reduced to 2.56 μA, which corroborates the evidence of electron transfer in this system.

3.7. Feasibility for practical applications

3.7.1. Influence of anions, HA, and water matrix

The influence of some common anions usually found in water on the degradation efficiency of the $PA@Hem_{700}$/PMS system was investigated (Fig. 6a). From this study, besides the bicarbonate ion (HCO_3^-), which reduced the efficiency of the system to 83.7 %, all other studied anions (i.e., NO_3^-, SO_4^{2-}, Cl^-, HPO_4^{2-}, and $H_2PO_4^-$) exerted a negligible influence on the degradation efficiency of the $PA@Hem_{700}$/PMS system. The ability of HCO_3^- to adversely affect the degradation process can be attributed to its ability to alter the system's pH to alkaline, which was not conducive to this process. In addition, HCO_3^- can react with both $^{\bullet}OH$ and $SO_4^{\bullet -}$ radicals to produce carbonate radicals ($CO_3^{\bullet -}$) (Eqs. 7 and 8), which have less oxidation potential towards organic contaminants (Bae et al., 2024; Lutze et al., 2015).

$$HCO_3^- + {}^{\cdot}O\ H \rightarrow CO_3^{\cdot -} + H_2O \tag{7}$$

$$HCO_3^- + SO_4^{\cdot} \rightarrow CO_3^{\cdot -} + HSO_4^- \tag{8}$$

The possible impact of organic matter on the degradation efficiency of this system was assessed using HA. From the results of this study, as illustrated in Fig. 6a, the presence of HA in the system slightly reduced the efficiency to 90.2 %. This slight reduction could be attributed to the surface interaction between HA and the $PA@Hem_{700}$ surface, which reduces the number of active sites available for the adsorption of DCF. Similar results were made by Annamalai and Shin (2023) in their study on DCF degradation using boron-doped biochar derived from *Undaria pinnatifida* biomass as a catalyst. To further verify the prospects of this degradation system for practical applications, the study was conducted using different water matrices such as groundwater (GW), tap water (TW), and river water (RW). The physicochemical properties of these water matrices are presented in Table S5. As illustrated in Fig. 6b, the

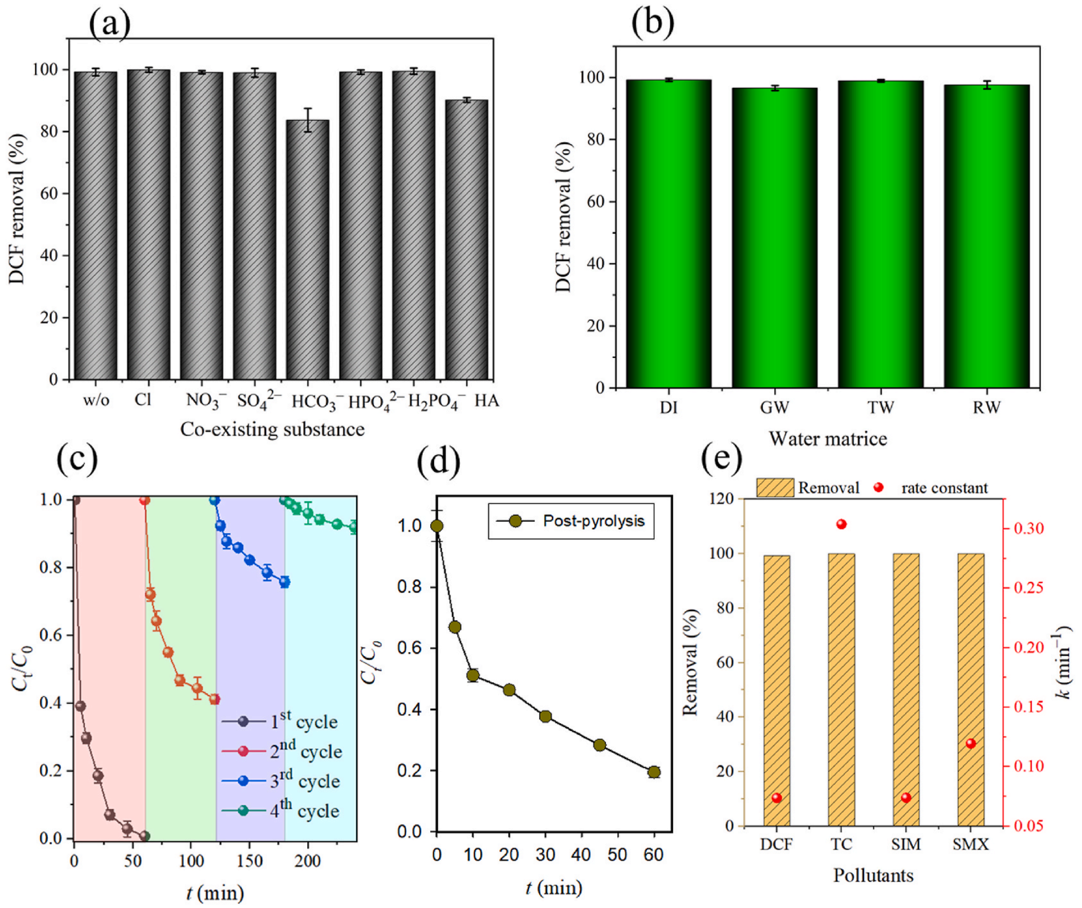

Fig. 6. Effects of (a) anions and HA; (b) water matrix on the removal of DCF; (c) degradation and reusability efficiency of PA@Hem$_{700}$/PMS system towards DCF removal; (d) DCF degradation with PA@Hem$_{700}$ (post-pyrolysis at 400 °C); (e) the removal efficiency of PA@Hem$_{700}$/PMS system towards the studied organic pollutants and their associated rate constant values. (Experimental conditions: $[\text{Catalyst}]_0 = 0.1$ g L^{-1}, $[\text{DCF}]_0 = 10$ mg L^{-1}, $[\text{PMS}]_0 = 1.0$ mM, pH = 6.01; $[\text{Anions}]_0 = 20$ mM; $[\text{TC}]_0 = [\text{SMX}]_0 = 0.02$ mM, $[\text{SMZ}]_0 = 0.05$ mM).

PA@Hem$_{700}$/PMS system exhibited excellent degradation efficiency towards DCF in all water matrices studied (≥96 %). The calculated k values for the degradation of DCF in these matrices were in the order k_{DI} (7.36×10^{-2} min^{-1}) > k_{GW} (6.20×10^{-2} min^{-1}) > k_{TW} (6.11×10^{-2} min^{-1}) > k_{RW} (4.84×10^{-2} min^{-1}) (Fig. S5). These observations suggest that although the presence of anions has only a slight influence on the removal efficiency of the system, their overall effect on the degradation rate cannot be ignored. Cumulatively, these findings may suggest the potential of the PA@Hem$_{700}$/PMS system for the practical removal of DCF from various water matrices. Furthermore, the degradation efficiency of this catalyst was compared to other reported catalysts, as presented in Table S6. From this analysis, PA@Hem$_{700}$, as a catalyst, possesses an equally optimal DCF degradation efficiency. This, in addition to its magnetic properties and ability to degrade other organic pollutants, make it a suitable alternative for the practical remediation of organic pollutants in aqueous solution.

3.7.2. Reusability and stability studies

The ability of the catalyst to be reused for further catalytic degradation experiments was assessed, and the results are presented in Fig. 6c. From this data, the DCF removal decreased from 99.4 % to 58.8 %, 24.2 %, and 8.1 % in the second, third, and fourth cycle degradation experiments, respectively. This significant reduction could be attributed to the strong forces of attraction between the DCF degraded products to the and PA@Hem$_{700}$ active sites. This makes these active sites unavailable for further DCF removal cycles (Dai et al., 2024; Lach and Szymonik, 2020). To examine this catalytic deactivation, PA@Hem$_{700}$ sample after DCF degradation was studied by XPS (Fig. S6). The core level spectra of C 1s, O 1s, N 1s, and Fe 2p orbitals indicate PA@Hem$_{700}$ surface undergoes noticeable changes upon DCF oxidation. In particular, the spectral features of N 1s orbital (Fig. 7a) showed a huge variation to that of PA@Hem$_{700}$ before reaction (Fig. S3c). Deconvolution results revealed a notable difference in the distribution of N-coordination sites. As pyridinic-N sites play a key role in PMS activation, its population declines 15 % from the before reacted sample (Fig. 7b). This indicates that fading of catalytic activity after initial cycles might be linked to the coverage of these active centres by the degraded by-products. However, the catalytic performance of PA@Hem$_{700}$ after DCF degradation was partially restored by subjecting the used catalyst to low-temperature pyrolysis at 400 °C in N_2 atmosphere. The DCF degradation profile of this post pyrolysis catalyst showed 80 % DCF removal (Fig. 6d), further confirming that the deactivation was primarily due to the blocking reaction products on the active sites. Therefore, post thermal treatment is seem to be essential for PA@Hem$_{700}$ for maintaining decent catalytic performance over multiple cycles. The stability of the catalyst was further investigated by analysing the amount of Fe^{2+} leached at the end of each cycle using inductively coupled plasma-optical emission spectrometry (ICP-OES 5800, Agilent Technologies, USA). From this assessment, the Fe^{2+} concentrations detected were 0.12 and 0.05 mg L^{-1} after the first and second cycles, respectively; however, Fe^{2+} was not detected in the third cycle. Furthermore, a high recovery rate (i.e., >90 %) was recorded for the catalyst throughout the study. This could be due to its high magnetic properties and optimal stability, which facilitate its easy removal using a magnet.

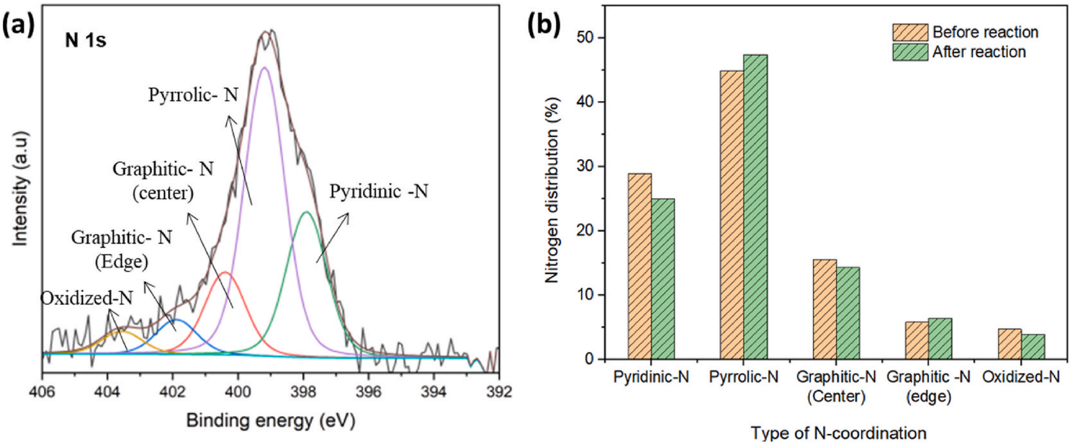

Fig. 7. (a) Deconvoluted XP spectra of N 1s orbital of PA@Hem$_{700}$ (after reaction), (b) the distribution of different N- functionals in before and after reacted PA@Hem$_{700}$ samples.

3.7.3. *Degradation efficiency against other organic contaminants*

The efficiency of the PA@Hem$_{700}$/PMS system against other organic pollutants was further assessed, and the results are presented in Fig. 6e. The HPLC conditions under which these pollutants were analysed are presented in Table S7. Here, SIM, TC, and SMX were selected due to their ability to represent a broad range of pollutants likely to be present in

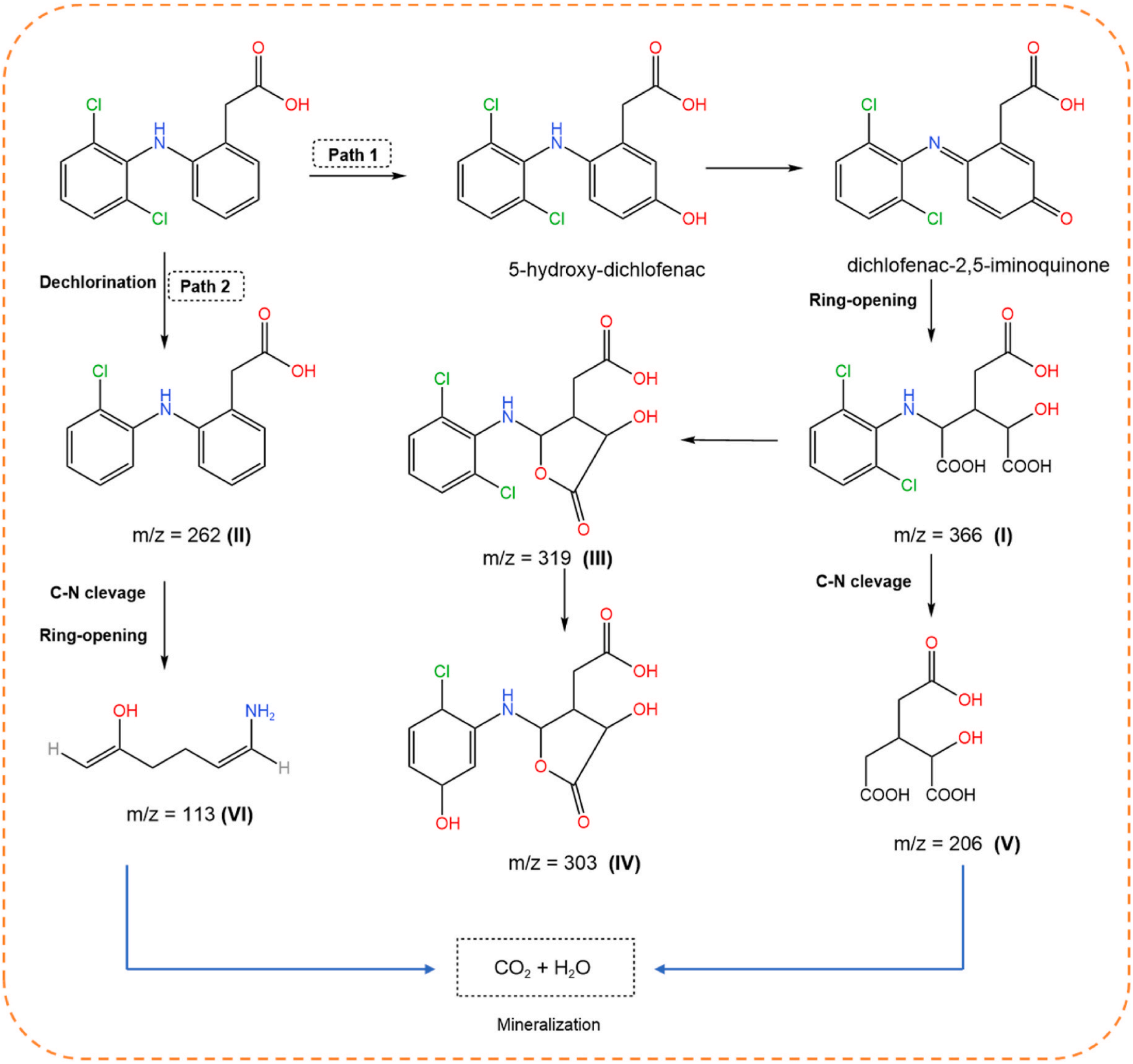

Fig. 8. Proposed DCF degradation pathway in PA@Hem$_{700}$/PMS system based on UHPLC-MS/MS results.

wastewater. From Figs. 6e and 100 % removal of TC was achieved within 20 min, whereas approximately 94.7 % and 100 % removal efficiencies of SIM and SMX, respectively, were achieved within 60 min. The k values for these degradation studies were 3.04×10^{-1}, 1.21×10^{-1}, 7.38×10^{-2}, and 7.36×10^{-2} min^{-1} for TC (log $K_{ow} = -1.3$), SMX (log $K_{ow} = 0.89$), SIM (log $K_{ow} = 2.18$), and DCF (log $K_{ow} = 4.0$), respectively. These findings suggest that the PA@Hem$_{700}$/PMS system accelerates the degradation of hydrophilic pollutants (Fig. S7). Further, the high pollutant removal % observed with PA@Hem$_{700}$/PMS system indicates its potential applicability for a broad range of organic contaminants.

3.8. Mineralization and DCF degradation pathway

To assess the mineralization of DCF in the degradation system, the amount of total organic carbon (TOC) removed after the degradation process was assessed, as described in **Text S8**. As shown in Fig. S8, the PA@Hem$_{700}$/PMS system achieved a TOC removal of 65.8 % after 60 min of reaction. This observation possibly verifies the assertion by several authors, such as Masud and Shin (2024) and Chen et al. (2016), who reported that the total removal of a pollutant does not infer complete mineralization. The TOC removal in this study was observed to be higher than that reported by Annamalai and Shin (2023); Dadban Shahamat et al. (2019); Wu et al. (2024); Xu et al. (2023), although these studies have comparable degradation efficiencies. In addition, compared to these reported studies, the PA@Hem$_{700}$ catalyst could be easily retrieved and recovered owing to its magnetic properties, which enhance its superiority.

The degradation pathway for DCF in the PA@Hem$_{700}$/PMS system and its intermediate products were assessed using ultra-HPLC-coupled mass spectroscopy (UHPLC-MS/MS). As observed from the chromatogram illustrated in Fig. S9, the peak intensity at the mass-to-charge ratio (m/z) value of 296 decreased significantly at the end of the reaction, suggesting the efficient degradation of DCF in the PA@Hem$_{700}$/PMS system. Comparing the identified products with previous reports of Aziz et al. (2019), Shi et al. (2019), and Xie et al. (2022), it is evident that the DCF degradation may involve hydroxylation, C–N bond cleavage, dehalogenation, and ring-opening reactions. Based on this, two degradation paths are proposed for DCF degradation in PA@Hem$_{700}$/PMS system (Fig. 8). In degradation path 1, the hydroxyl radicals attack the aromatic ring and form 5-hydroxy-diclofenac. With the involvement of $^1O_2$ species, the oxidation of DCF initiates at the hydroxyl position, which then reacts with oxygen and result in the diclofenac-2, 5-iminoquinone formation. Subsequently, this product undergoes ring opening reaction and forms (I) with $m/z = 366$. It can be seen that carboxyl groups in (I) undergoes ring closure to form a lactone derivative (III) having $m/z = 319$. On the other hand, the product (I) undergoes C–N bond cleavage to transform it towards a low molecular weight product (V) $m/z = 206$. In path 2, the DCF first undergoes dehalogenation by eliminating one Cl^- that lead to the formation of (II) with $m/z = 262$. The mass spectra result of 60 min duration sample revealed a prominent peak at $m/z = 113$, which likely occurs from sequential reactions steps that includes C–N cleavage and ring-opening of product (II) to form low molecular weight product (VI). Comparing these results with TOC removal it is clear that these ring-opened compounds (V and VI) undergoes further oxidation to mineralize it to CO_2, and H_2O in the PA@Hem$_{700}$/PMS system.

3.9. PA@Hem$_{700}$/PMS system limitations and guidance

- The major limitation of this study is the poor reusability efficiency of the catalyst. This aspect is very important for consideration of the catalyst for practical applications. To address this, it is recommended a method capable of regenerating the catalyst with associated high efficiency is developed to enhance the prospects of the catalyst for practical applications.
- Evaluation of the environmental risk of the treated solution towards some biological organisms such as microorganisms and plants can be assessed to confirm the benignity of the process.
- Additionally, a life cycle assessment may be needed to establish the environmental impact of the catalyst from its synthesis to end of life.

4. Conclusions

In this study we sucessfully demonstrated the fabrication of novel Fe/N-C catalyst (PA@Hem$_x$) using a mixture of hemin and polyacrylate precursors by adopting simple pyrolysis process. The characterization studies, such as XPS, Raman, FTIR, and XRD, confirmed the successful incorporation of hemin, forming a magnetic composite with enhanced surface defects. The PA@Hem$_{700}$ catalyst, achieved >99 % DCF removal and 65.8 % of TOC removal within 60 min. The PA@Hem$_{700}$/PMS exhibited a remarkable DCF removal performance over a broad range of pH in the presence of commonly existing anions and HA, including various water matrices. The results from quenching and ESR experiments indicate the presence of $^{\bullet}OH$, $SO_4^{\bullet-}$, and $^1O_2$, with the latter being the dominant ROS that is responsible for DCF degradation process. The participation of electron transfer in the degradation process was also confirmed using the electrochemical impedance spectroscopy and chronoamperometry analysis. Finally, determining the intermediate products via LC-MS/MS analysis elucidated the plausible degradation pathway. The results of this study shows PA@Hem$_{700}$ has excellent prospects for the degradation of a wide range of organic pollutants, further promoting its practicability in wastewater treatment.

CRediT authorship contribution statement

Aaron Albert Aryee: Writing – original draft, Investigation, Formal analysis, Data curation, Conceptualization. **Alam Venugopal Narendra Kumar:** Data curation, Formal analysis, Investigation, Methodology, Software, Writing – review & editing. **Won Sik Shin:** Writing – review & editing, Validation, Supervision, Resources, Project administration, Funding acquisition.

Declaration of competing interest

The authors declare that they have no known competing financial interests or personal relationships that could have appeared to influence the work reported in this paper.

Acknowledgement

This work was supported by the National Research Foundation of Korea (NRF) grant funded by the Korean government (MSIT) (No. 2022R1A2C2091561).

Appendix A. Supplementary data

Supplementary data to this article can be found online at https://doi.org/10.1016/j.chemosphere.2025.144388.

Data availability

Data will be made available on request.

References

Aguinaco, A., Beltrán, F.J., García-Araya, J.F., Oropesa, A., 2012. Photocatalytic ozonation to remove the pharmaceutical diclofenac from water: influence of variables. Chem. Eng. J. 189–190, 275–282. https://doi.org/10.1016/j.cej.2012.02.072.

Alessandretti, I., Rigueto, C.V.T., Nazari, M.T., Rosseto, M., Dettmer, A., 2021. Removal of diclofenac from wastewater: a comprehensive review of detection, characteristics and tertiary treatment techniques. J. Environ. Chem. Eng. 9 (6), 106743. https://doi.org/10.1016/j.jece.2021.106743.

Alimi, O.S., Fadare, O.O., Okoffo, E.D., 2021. Microplastics in African ecosystems: current knowledge, abundance, associated contaminants, techniques, and research needs. Sci. Total Environ. 755, 142422. https://doi.org/10.1016/j.scitotenv.2020.142422.

Amrutha, Jeppu, G., Girish, C.R., Prabhu, B., Mayer, K., 2023. Multi-component adsorption isotherms: review and modeling studies. Environ. Proc. 10, 38. https://doi.org/10.1007/s40710-023-00631-0.

Annamalai, S., Shin, W.S., 2023. Algae-derived metal-free boron-doped biochar acts as a catalyst for the activation of peroxymonosulfate toward the degradation of diclofenac. Environ. Pollut. 331, 121850. https://doi.org/10.1016/j.envpol.2023.121850.

Aryee, A.A., Han, R., Qu, L., 2022. Occurrence, detection and removal of amoxicillin in wastewater: a review. J. Clean. Prod. 368, 133140. https://doi.org/10.1016/j.jclepro.2022.133140.

Aryee, A.A., Ma, Y., Wang, J., Han, R., Qu, L., 2023. A magnetic biomass/MOF composite as a functional material for the oxidative removal of tetracycline: degradation mechanism and toxicity study. J. Environ. Chem. Eng. 11, 110663. https://doi.org/10.1016/j.jece.2023.110663.

Aryee, A.A., Masud, M.A. Al, Shin, W.S., 2024. Enhanced simazine degradation via peroxymonosulfate activation using hemin-doped rice husk biochar as a novel Fe/N–C catalyst. Chemosphere 366, 143549. https://doi.org/10.1016/j.chemosphere.2024.143549.

Aryee, A.A., Mpatani, F.M., Dovi, E., Li, Q., Wang, J., Han, R., Li, Z., Qu, L., 2021. A novel antibacterial biocomposite based on magnetic peanut husk for the removal of trimethoprim in solution: adsorption and mechanism study. J. Clean. Prod. 329, 129722. https://doi.org/10.1016/j.jclepro.2021.129722.

Ayiania, M., Smith, M., Hensley, A.J.R., Scudiero, L., McEwen, J.-S., Garcia-Perez, M., 2020. Deconvoluting the XPS spectra for nitrogen-doped chars: an analysis from first principles. Carbon 162, 528–544. https://doi.org/10.1016/j.carbon.2020.02.065.

Aziz, K.H.H., Mustafa, F.S., Hassan, M.A., Omer, K.M., Hama, S., 2024. Biochar as green adsorbents for pharmaceutical pollution in aquatic environments: a review. Desalination 583, 117725. https://doi.org/10.1016/j.desal.2024.117725.

Aziz, K.H.H., Omer, K.M., Mahyar, A., Miessner, H., Mueller, S., Moeller, D., 2019. Application of photocatalytic falling film reactor to elucidate the degradation pathways of pharmaceutical diclofenac and ibuprofen in aqueous solutions. Coatings 9 (8), 465. https://doi.org/10.3390/coatings9080465.

Bae, S., Masud, M.A. Al, Annamalai, S., Shin, W.S., 2024. The inherent nature of N/P heteroatoms in *Sargassum fusiforme* seaweed biochar enhanced the nonradical activation of peroxymonosulfate for acetaminophen degradation in aquatic environments. Chemosphere 356, 141877. https://doi.org/10.1016/j.chemosphere.2024.141877.

Boitrel, B., Hijazi, I., Roisnel, T., Oohora, K., Hayashi, T., 2017. Iron-strapped porphyrins with carboxylic acid groups hanging over the coordination site: synthesis, X-ray characterization, and dioxygen binding. Inorg. Chem. 56, 7373–7383. https://doi.org/10.1021/acs.inorgchem.7b00343ï.

Cangola, J., Abagale, F.K., Cobbina, S.J., 2024. A systematic review of pharmaceutical and personal care products as emerging contaminants in waters: the panorama of West Africa. Sci. Total Environ. 911, 168633. https://doi.org/10.1016/j.scitotenv.2023.168633.

Chen, W., Li, X., Pan, Z., Ma, S., Li, L., 2016. Effective mineralization of diclofenac by catalytic ozonation using Fe-MCM-41 catalyst. Chem. Eng. J. 304, 594–601. https://doi.org/10.1016/j.cej.2016.06.139.

Dadban Shahamat, Y., Zazouli, M.A., Zare, M.R., Mengelizadeh, N., 2019. Catalytic degradation of diclofenac from aqueous solutions using peroxymonosulfate activated by magnetic MWCNTs-$CoFe_3O_4$ nanoparticles. RSC Adv. 9, 16496–16508. https://doi.org/10.1039/C9RA02757B.

Dai, K., Chen, L., Aryee, A.A., Yang, P., Han, R., Qu, L., 2024. Adsorption studies of tetracycline hydrochloride and diclofenac sodium on NH2-MIL-53(Al/Zr) sodium alginate gel spheres. Int. J. Biol. Macromol. 271, 132637. https://doi.org/10.1016/j.ijbiomac.2024.132637.

Di Maggio, R., Dirè, S., Callone, E., Bergamonti, L., Lottici, P.P., Albatici, R., Rigon, R., Ataollahi, N., 2019. Super-adsorbent polyacrylate under swelling in water for passive solar control of building envelope. SN Appl. Sci. 2, 45. https://doi.org/10.1007/s42452-019-1814-4.

Giannakis, S., Lin, K.-Y.A., Ghanbari, F., 2021. A review of the recent advances on the treatment of industrial wastewaters by sulfate radical-based advanced oxidation processes (SR-AOPs). Chem. Eng. J. 406, 127083. https://doi.org/10.1016/j.cej.2020.127083.

Gu, Y., Yang, M., Wang, W., Han, R., 2019. Phosphate adsorption from solution by zirconium-loaded carbon nanotubes in batch mode. J. Chem. Eng. Data 64, 2849–2858. https://doi.org/10.1021/acs.jced.9b00214.

Han, Z., Li, J., Han, X., Zhao, X., Ji, X., 2018. A novel biomimetic catalyst constructed by axial coordination of hemin with PAN fiber for efficient degradation of organic dyes. J. Mater. Sci. 53, 4118–4131. https://doi.org/10.1007/s10853-017-1899-3.

Hao, L., Zhang, J., Liu, J., Min, Y., Chen, C., 2023. Applications of carbon-based materials in activated peroxymonosulfate for the degradation of organic pollutants: a review. Chem. Rec. 23, e202300203. https://doi.org/10.1002/tcr.202300203.

Hassani, A., Scaria, J., Ghanbari, F., Nidheesh, P.V., 2023. Sulfate radicals-based advanced oxidation processes for the degradation of pharmaceuticals and personal care products: a review on relevant activation mechanisms, performance, and perspectives. Environ. Res. 217, 114789. https://doi.org/10.1016/j.envres.2022.114789.

Hu, Y., Han, R., 2019. Selective and efficient removal of anionic dyes from solution by zirconium(iv) hydroxide-coated magnetic materials. J. Chem. Eng. Data 64, 791–799. https://doi.org/10.1021/acs.jced.8b01063.

Jiang, C., Hou, M., Yang, L., Guo, S., Yang, G., Xing, B., Wang, Y., Wang, D., Shi, X., 2024. High efficiency degradation organic pollutant using novel heme-derived Fe–N co-doped carbon catalyst activated PDS and H_2O_2. J. Phys. Chem. C 128, 4459–4469. https://doi.org/10.1021/acs.jpcc.3c07149.

Lach, J., Szymonik, A., 2020. Adsorption of diclofenac sodium from aqueous solutions on commercial activated carbons. Desal. Water Treat. 186, 418–429. https://doi.org/10.5004/dwt.2020.25567.

Lee, Y. Bin, Narendra Kumar, A.V., Shin, W.S., 2023. Transforming diapers into inorganic carbonate enriched carbon catalyst for improved trimethoprim degradation performance. Compos. B Eng. 267, 111051. https://doi.org/10.1016/j.compositesb.2023.111051.

Li, W., Orozco, R., Camargos, N., Liu, H., 2017. Mechanisms on the impacts of alkalinity, pH, and chloride on persulfate-based groundwater remediation. Environ. Sci. Technol. 51, 3948–3959. https://doi.org/10.1021/acs.est.6b04849.

Li, X., Shen, X., Jiang, W., Xi, Y., Li, S., 2024. Comprehensive review of emerging contaminants: detection technologies, environmental impact, and management strategies. Ecotoxicol. Environ. Saf. 278, 116420. https://doi.org/10.1016/j.ecoenv.2024.116420.

Liu, M., Zhang, X., Li, Z., Qu, L., Han, R., 2020. Fabrication of zirconium (IV)-Loaded chitosan/Fe_3O_4/graphene oxide for efficient removal of alizarin red from aqueous solution. Carbohydr. Polym. 248, 116792. https://doi.org/10.1016/j.carbpol.2020.116792.

Lu, X., Shao, Y., Gao, N., Chen, J., Zhang, Y., Xiang, H., Guo, Y., 2017. Degradation of diclofenac by UV-activated persulfate process: kinetic studies, degradation pathways and toxicity assessments. Ecotoxicol. Environ. Saf. 141, 139–147. https://doi.org/10.1016/j.ecoenv.2017.03.022.

Lutze, H.V., Kerlin, N., Schmidt, T.C., 2015. Sulfate radical-based water treatment in presence of chloride: formation of chlorate, inter-conversion of sulfate radicals into hydroxyl radicals and influence of bicarbonate. Water Res. 72, 349–360. https://doi.org/10.1016/j.watres.2014.10.006.

Masud, M.A. Al, Shin, W.S., 2024. Recycling of spent superabsorbent polymer into nitrogen-doped carbon catalyst for enhanced antibiotic degradation in groundwater. J. Water Proc. Eng. 64, 105567. https://doi.org/10.1016/j.jwpe.2024.105567.

Masud, M.A. Al, Shin, W.S., Kim, D.G., 2023. Fe-doped kelp biochar-assisted peroxymonosulfate activation for ciprofloxacin degradation: multiple active site-triggered radical and non-radical mechanisms. Chem. Eng. J. 471, 144519. https://doi.org/10.1016/j.cej.2023.144519.

Mustafa, F.S., Hama Aziz, K.H., 2023. Heterogeneous catalytic activation of persulfate for the removal of rhodamine B and diclofenac pollutants from water using iron-impregnated biochar derived from the waste of Black seed pomace. Process Saf. Environ. Prot. 170, 436–448. https://doi.org/10.1016/j.psep.2022.12.030.

Peng, Y., Tang, H., Yao, B., Gao, X., Yang, X., Zhou, Y., 2021. Activation of peroxymonosulfate (PMS) by spinel ferrite and their composites in degradation of organic pollutants: a review. Chem. Eng. J. 414, 128800. https://doi.org/10.1016/j.cej.2021.128800.

Pereira, F.J., López, R., Ferrer, N., Prieto, A.C., Nogal, R.A., Nodar, A., Aller, A.J., 2021. A comparative appraisal of Raman band ratioing and chemometric analysis for classification of ancient papyri. J. Cult. Herit. 52, 55–64. https://doi.org/10.1016/j.culher.2021.09.003.

Sathishkumar, P., Meena, R.A.A., Palanisami, T., Ashokkumar, V., Palvannan, T., Gu, F. L., 2020. Occurrence, interactive effects and ecological risk of diclofenac in environmental compartments and biota - a review. Sci. Total Environ. 698, 134057. https://doi.org/10.1016/j.scitotenv.2019.134057.

Shi, H., Zhou, G., Liu, Y., Fu, Y., Wang, H., Wu, P., 2019. Kinetics and pathways of diclofenac degradation by heat-activated persulfate. RSC Adv. 9, 31370–31377. https://doi.org/10.1039/C9RA05034E.

Shukla, S., Khan, R., Saxena, A., Sekar, S., 2022. Microplastics from face masks: a potential hazard post Covid-19 pandemic. Chemosphere 302, 134805. https://doi.org/10.1016/j.chemosphere.2022.134805.

Song, W., Xiao, X., Wang, G., Dong, X., Zhang, X., 2023. Highly efficient peroxymonosulfate activation on Fe-N-C catalyst via the collaboration of low-coordinated Fe-N structure and Fe nanoparticles for enhanced organic pollutant degradation. J. Hazard Mater. 455, 131596. https://doi.org/10.1016/j.jhazmat.2023.131596.

Su, Y., Jassby, D., Song, S., Zhou, X., Zhao, H., Filip, J., Petala, E., Zhang, Y., 2018. Enhanced oxidative and adsorptive removal of diclofenac in heterogeneous Fenton-like reaction with sulfide modified nanoscale zerovalent iron. Environ. Sci. Technol. 52, 6466–6475. https://doi.org/10.1021/acs.est.8b00231.

Wang, J., Guo, X., 2020a. Adsorption kinetic models: physical meanings, applications, and solving methods. J. Hazard Mater. 390, 122156. https://doi.org/10.1016/j.jhazmat.2020.122156.

Wang, J., Guo, X., 2020b. Adsorption isotherm models: classification, physical meaning, application and solving method. Chemosphere 258, 127279. https://doi.org/10.1016/j.chemosphere.2020.127279.

Wu, G., Wang, J., Wan, Q., Cao, S., Huang, T., Lu, J., Ma, J., Wen, G., 2023. Kinetics and mechanism of sulfate radical-and hydroxyl radical-induced disinfection of bacteria and fungal spores by transition metal ions-activated peroxymonosulfate. Water Res. 243, 120378. https://doi.org/10.1016/j.watres.2023.120378.

Wu, Y., Zheng, J., Liu, J., Lin, Q., Zeng, C., Liu, Y., Luo, H., Luo, Y., Pan, J., Xie, H., 2024. Degradation of diclofenac sodium by peroxymonosulfate activated with a sulfur-doped chitosan ferrocarbon material: synergistic interaction of free radical and nonfree radical pathways. J. Colloid Interface Sci. 680, 734–747. https://doi.org/10.1016/j.jcis.2024.11.122.

Xie, J., Xu, P., Liu, M., Liu, Y., Zhu, L., Yu, F., Zhang, P., Li, J., Luo, Y., Zhou, B., 2022. Anchoring phosphorus on in-situ nitrogen-doped biochar by mechanical milling for promoted electron transfer from diclofenac sodium to peroxymonosulfate. Sep. Purif. Technol. 301, 121964. https://doi.org/10.1016/j.seppur.2022.121964.

Xu, L., Ye, Z., Pan, Y., Zhang, Y., Gong, H., Mei, X., Qiao, W., Gan, L., 2023. Effect of lignocellulosic biomass composition on the performance of biochar for the activation of peroxymonosulfate to degrade diclofenac. Sep. Purif. Technol. 311, 123312. https://doi.org/10.1016/j.seppur.2023.123312.

Zhang, H., Guan, W., Zhang, L., Guan, X., Wang, S., 2020. Degradation of an organic dye by bisulfite catalytically activated with iron manganese oxides: the role of superoxide radicals. ACS Omega 5, 18007–18012. https://doi.org/10.1021/acsomega.0c01257.

Zhang, X., Gao, C., Wang, R., Aryee, A.A., Han, R., 2023. Study on adsorption of salicylic acid and sulfosalicylic acid by MOF–sodium alginate gel beads obtained in a green way. Int. J. Biol. Macromol. 253, 127535. https://doi.org/10.1016/j.ijbiomac.2023.127535.